

## Article

# Complete Elimination of the Ciprofloxacin Antibiotic from Water by the Combination of Adsorption–Photocatalysis Process Using Natural Hydroxyapatite and TiO<sub>2</sub>

Sabrina Cheikh <sup>1,2</sup>, Ali Imessaoudene <sup>1</sup>, Jean-Claude Bollinger <sup>3</sup>, Amina Hadadi <sup>1</sup>, Amar Manseri <sup>4</sup>, Abdelkrim Bouzaza <sup>5</sup>, Aymen Assadi <sup>5,\*</sup>, Abdeltif Amrane <sup>5</sup>, Meriem Zamouche <sup>6</sup>, Atef El Jery <sup>7,8</sup> and Lotfi Mouni <sup>1,\*</sup>

- <sup>1</sup> Laboratoire de Gestion et Valorisation des Ressources Naturelles et Assurance Qualité, Faculté SNVST, Université de Bouira, Bouira 10000, Algeria
  - <sup>2</sup> Département de Génie des Procédés, Faculté de Technologie, Université de Bejaia, Bejaia 06000, Algeria
  - <sup>3</sup> Laboratoire E2Lim, Université de Limoges, 123 Avenue Albert Thomas, 87060 Limoges, France
  - <sup>4</sup> Centre de Recherche en Technologie des Semi-Conducteurs pour l’Énergétique, 02 Bd Frantz Fanon, B.P. 140 Algiers 7, Merveilles 16038, Algeria
  - <sup>5</sup> Ecole Nationale Supérieure de Chimie de Rennes, Université de Rennes, CNRS, ISCR—UMR 6226, 35000 Rennes, France
  - <sup>6</sup> Laboratory of Engineering and Processes of Environment (LIPE), Faculty of Process Engineering, University of Constantine 3, Constantine 25000, Algeria
  - <sup>7</sup> Department of Chemical Engineering, College of Engineering, King Khalid University, Abha 61411, Saudi Arabia
  - <sup>8</sup> National Engineering School of Gabes, Gabes University, Ibn El Khattab Street, Zrig Gabes 6029, Tunisia
- \* Correspondence: aymen.assadi@ensc-rennes.fr (A.A.); l.mouni@univ-bouira.dz (L.M.)



**Citation:** Cheikh, S.; Imessaoudene, A.; Bollinger, J.-C.; Hadadi, A.; Manseri, A.; Bouzaza, A.; Assadi, A.; Amrane, A.; Zamouche, M.; El Jery, A.; et al. Complete Elimination of the Ciprofloxacin Antibiotic from Water by the Combination of Adsorption–Photocatalysis Process Using Natural Hydroxyapatite and TiO<sub>2</sub>. *Catalysts* **2023**, *13*, 336. <https://doi.org/10.3390/catal13020336>

Academic Editor: Roberto Fiorenza

Received: 24 December 2022

Revised: 19 January 2023

Accepted: 27 January 2023

Published: 2 February 2023



**Copyright:** © 2023 by the authors. Licensee MDPI, Basel, Switzerland. This article is an open access article distributed under the terms and conditions of the Creative Commons Attribution (CC BY) license (<https://creativecommons.org/licenses/by/4.0/>).

**Abstract:** The main objective of this work was to assess the performance of combined processes, adsorption/ photodegradation of the ciprofloxacin antibiotic (CIP). Adsorption was achieved on natural hydroxyapatite (*nat-HA*) in the batch mode. The effect of pH (3–12), initial ciprofloxacin concentration ( $C_0$ , 25–200 mg L<sup>-1</sup>), adsorbent dose ( $m$ , 0.25–3 g L<sup>-1</sup>), and temperature ( $T$ , 298–328 K) on the ciprofloxacin adsorption capacity was studied. At 298 K, the maximum uptake of 147.7 mg g<sup>-1</sup> was observed with pH close to 8, 1 g L<sup>-1</sup> *nat-HA* dose, and 150 mg L<sup>-1</sup> initial CIP concentration. Adsorption was effective, with a removal percentage of 82% within 90 minutes of contact time. For ciprofloxacin adsorption onto *nat-HA*, a pseudo-second-order kinetic model is well-suited. The Langmuir isotherm model successfully fit the experimental data and the process was spontaneous and exothermic. The coupling processes (adsorption/photocatalysis) were examined and found to be highly effective. For the remaining concentrations, the maximum degradation efficiency and mineralization yield were ~100% and 98.5%, respectively, for 1 mg L<sup>-1</sup> initial CIP. The combination of the strong adsorption capacity of natural hydroxyapatite and the high photocatalytic activity of TiO<sub>2</sub> can be an effective technique for removing fluoroquinolone antibiotics from wastewater.

**Keywords:** natural hydroxyapatite; ciprofloxacin; adsorption; TiO<sub>2</sub>; photodegradation; UV light

## 1. Introduction

The presence of antibiotics in surface water and wastewater has been frequently observed [1–3] and is becoming an increasing issue due to their toxicological effect on aquatic species and the resistance they can cause in some bacterial strains, even at low concentrations [4]. Fluoroquinolones are the antibiotics most commonly used in human and veterinary medicine [5]. However, antibiotics are frequently detected in the final effluents of wastewater treatment plants (WWTPs) because of their extensive use [6].

Ciprofloxacin (CIP; C<sub>17</sub>H<sub>18</sub>O<sub>3</sub>N<sub>3</sub>F) is a zwitterionic antibiotic that is classified as a fluoroquinolone of the second generation that is in widespread use. It is effective against a

wide variety of Gram-negative and Gram-positive bacteria [6,7]. As a result of its extensive use to treat a variety of human and animal ailments, CIP is regularly identified in ground-water and contaminated wastewater [8,9]. The transfer of the CIP antibiotic into aquatic habitats poses a major risk to human health and ecological systems due to the development of resistant strains via chromosomal alterations and chronic allergic reactions [10,11]. From the toxicological standpoint, CIP was identified as a newly developing genotoxic and mutagenic micropollutant [12]. Due to its bacteria-inhibiting properties, the CIP antibiotic demonstrates low biodegradability in ecosystems, which results in a higher tendency to survive and accumulate in the environment [13,14]. Before being discharged into waterbodies, effluents containing the CIP antibiotic must be adequately cleansed [15]. Consequently, removing CIP from water has become a task of increasing significance and urgency.

In order to treat CIP in contaminated water, several conventional techniques, such as adsorption, oxidation [16,17], oxidation by chlorination [18], ozonation [19], photolytic and photocatalytic treatment [20,21], and biological treatment [22,23] are commonly used. Among all the procedures listed, adsorption is the most effective method for removing antibiotics from pharmaceutical wastewater [24]. Due to its simplicity, quick recovery, high efficiency, and reusability of the adsorbent, it is the most promising technique [25]. The selection of adsorbents is crucial to achieving the highest removal efficiency by adsorption. Different adsorbents, such as clay minerals [26], graphene-based nanocomposites [27], activated carbon [28], biomass [29], and hydroxyapatites [30,31] have been recently exploited for the removal of antibiotics from water, as indicated in the pertinent literature.

Hydroxyapatite (HA,  $\text{Ca}_{10}(\text{PO}_4)_6(\text{OH})_2$ ) is a calcium phosphate-based substance with promising physicochemical qualities, such as high absorption capacity, low solubility, porous structure, non-toxicity, and good chemical stability [31]. Therefore, several technical applications involving HA-based materials have been studied, including gas detection, drug delivery and wastewater purification [32–34], tissue engineering [35].

Photocatalysis is a complimentary technique to conventional methods such as precipitation, electrocoagulation, flocculation, membrane or adsorption processes [36]. It is very effective at low concentrations and can be used at the end of the water treatment chain [37]. It aims for high mineralization of organic contaminants into  $\text{CO}_2$ ,  $\text{H}_2\text{O}$ , and mineral compounds by  $\text{OH}^\bullet$  and/or  $\text{O}_2^{\bullet-}$  [38]. In environmental engineering, photocatalysis is a viable alternative that is now being used on industrial pilot stages [39]. However, its application is restricted to low effluent concentrations. In fact, high concentrations of antibiotics inhibit the process greatly by preventing light from reaching the catalyst powder [40].

The principal goals of this study were (i) to study the removal of CIP by combining adsorption (hydroxyapatite) and photocatalysis ( $\text{TiO}_2$ ); (ii) in addition, the adsorption mechanism, kinetics, and thermodynamics were studied. Photocatalysis reduces the residual concentration to levels below the World Health Organization's (WHO) regulations [41].

## 2. Results and Discussion

### 2.1. Characterization

The nature of the solid phase and purity of the derived *nat*-HA crystals were confirmed using XRD analysis. Figure 1 represents the different prominent XRD peaks, d-spacing, and relative intensity which correspond to the planes (2 1 1), (3 0 0), (1 1 2), (2 1 3), (2 2 2), (3 1 0), (0 0 2), and (2 0 2) of the annealed bone at 800 °C compared with the standard JCPDS data for stoichiometric HA [42].

The FT-IR spectrum of the *nat*-HA (Figure 2) was well-defined, with peaks at 3592 and 655  $\text{cm}^{-1}$  corresponding to the stretching vibrations of  $\text{OH}^-$  groups. The peaks at 1090 and 962  $\text{cm}^{-1}$  were ascribed to the phosphate stretching vibration, and those observed at 605, 570, and 475  $\text{cm}^{-1}$  were assigned to the phosphate bending vibration. The peak at 1630  $\text{cm}^{-1}$  was ascribed to the adsorbed water molecules.

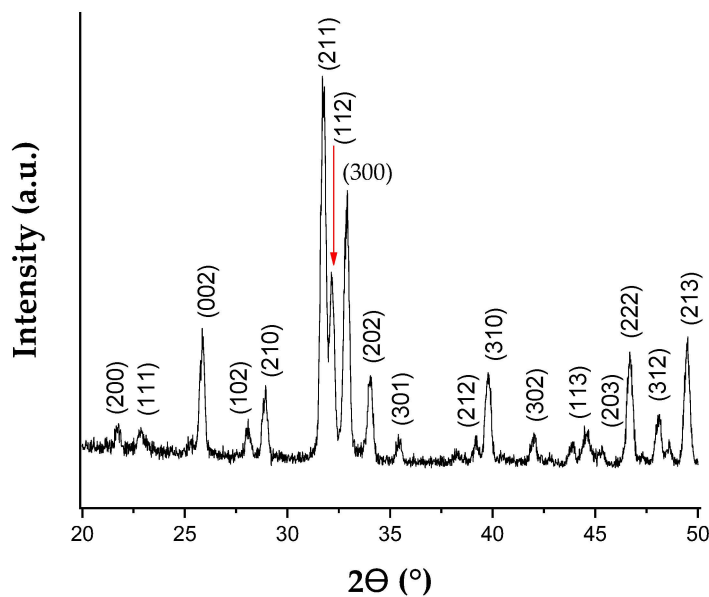


Figure 1. XRD pattern of natural hydroxyapatite.

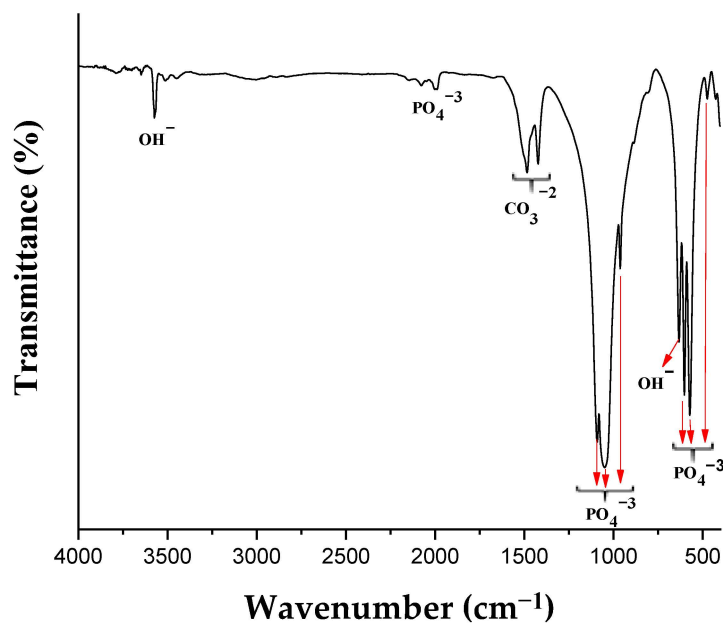
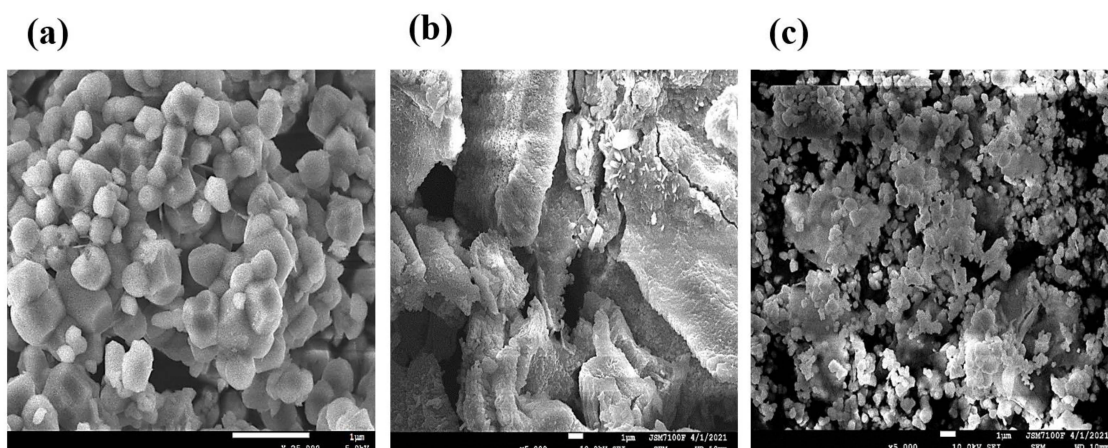


Figure 2. FTIR spectra of *nat-HA*.

The low intensity peak of carbonate groups was identified in the FTIR spectra at  $1482\text{ cm}^{-1}$  due to asymmetric stretching of the  $\text{CO}_3^{2-}$  group. The observed bands are in close accordance with *nat-HA* data reported in the literature [42,43].

The surface morphology and crystal size of the *nat-HA* were characterized by using SEM analysis. The SEM images of the bovine bone at  $800\text{ }^\circ\text{C}$  before and after ciprofloxacin adsorption are shown in Figure 3a–c, respectively. The *nat-HA* powder shows that the nanoparticles had irregular shapes. Although the morphology of the particles was observed to be very similar to irregular hexagons, they also contained small spheres and were agglomerated together in some parts. It may have occurred due to the interconnection of *nat-HA* particles [44]. The particle size is determined as approximately  $0.1\text{--}1\text{ }\mu\text{m}$ . Surface morphological changes of the *nat-HA* after ciprofloxacin adsorption showed no significant modification on the surface (Figure 3c).



**Figure 3.** SEM images of natural hydroxyapatite before ((a)  $\times 25,000$ ; (b)  $\times 5000$ ) and after ((c)  $\times 5000$ ) ciprofloxacin adsorption; pH = 8,  $C_0 = 200 \text{ mg L}^{-1}$ ,  $m = 1 \text{ g L}^{-1}$ , and  $T = 298 \text{ K}$ .

In Figure 4,  $\text{pH}_{\text{PZC}}$  is determined and reported. The result confirmed that the *nat-HA* surface is positively charged at pH levels less than 10.50, and vice versa.

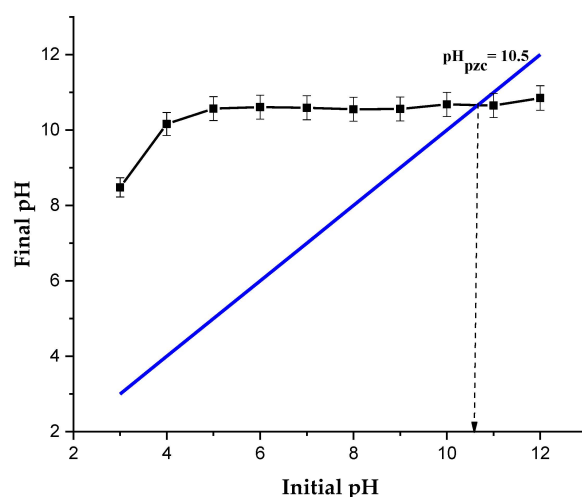


**Figure 4.** *nat-HA*:  $\text{pH}_{\text{PZC}}$  determination.

## 2.2. Adsorption Experiments

The parametric analysis allows for the determination of the most important factors favorable for the removal of CIP by adsorption on *nat-HA*, namely the pH, initial CIP concentration, contact time, and adsorbent dose.

### 2.2.1. Effect of the Initial pH and the Binding Mechanism

One of the most essential parameters affecting the adsorption process is the pH of a solution. Figure 5b illustrates the influence of pH (ranging from 3 to 12) on CIP adsorption onto *nat-HA* (at an initial CIP concentration of  $150 \text{ mg L}^{-1}$ , adsorbent dosage of  $1 \text{ g L}^{-1}$ , contact period of 3 h, and temperature of  $25 \text{ }^\circ\text{C}$ ). The pH is adjusted by adding HCl (0.1 M) and NaOH (0.1 M). After the equilibrium was achieved, samples were obtained for analysis. Solution pH is a crucial control parameter that influences the ionic speciation of adsorbate molecules as well as the surface charge of the adsorbent [15]. Figure 5a illustrates the distribution of CIP species at different pH levels. Consequently, CIP exists in three ionization states: cationic form ( $\text{CIP}^+$ ) at  $\text{pH} < 6.1$ , zwitterionic ( $\text{CIP}^\pm$ )—at  $\text{pH}$  between 6.1 and 8.9, and anionic ( $\text{CIP}^-$ )—at  $\text{pH} > 8.9$  [42].

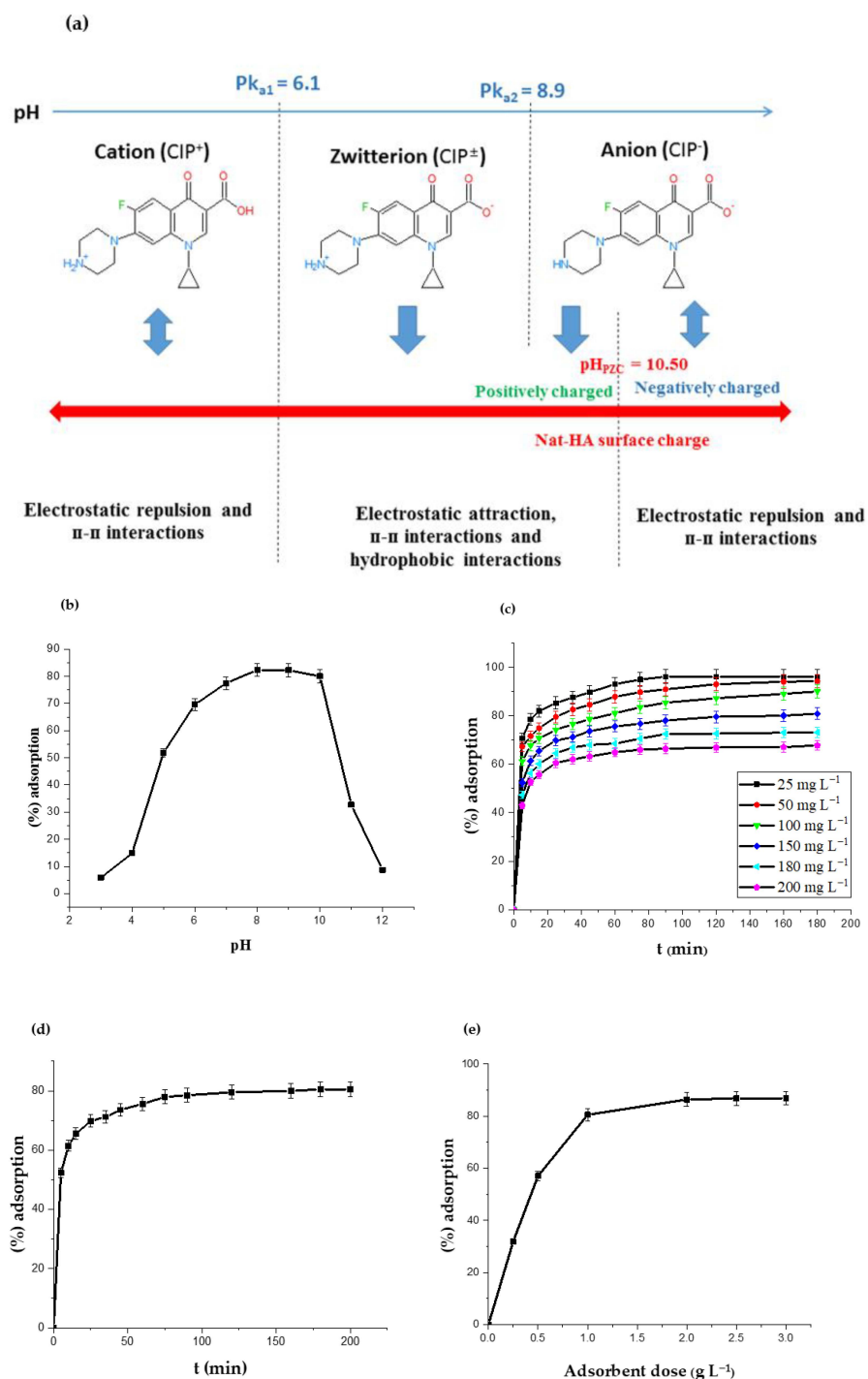
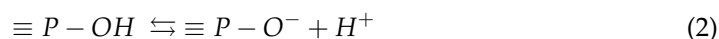
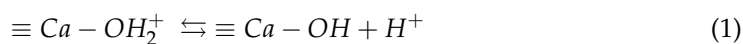


**Figure 5.** Physical parameters influencing CIP adsorption on *nat*-HA: (a) proposed adsorption mechanism, (b) initial pH, (c) initial concentration of CIP, (d) contact time, and (e) adsorbent dose.

Over the broad pH range of 3–12, the surface charge of the *nat*-HA adsorbent was examined. Based on Figure 4, the  $pH_{PZC}$  of *nat*-HA was determined to be 10.5.

At  $pH < pH_{PZC}$ , the *nat*-HA surface is protonated by hydrogen ions and becomes positively charged ( $nat\text{-}HA\text{-}H^+$ ). At  $pH > pH_{PZC}$ , the hydroxyl groups on the surface of *nat*-HA are deprotonated, resulting in a negatively charged surface ( $nat\text{-}HA^-$ ). At pH values close to  $pH_{PZC}$ , the *nat*-HA surface balances cationic and anionic active sites.

The following Equations (1)–(2) depict the protonation/deprotonation of *nat-HA* surface functional groups [45]:



The effect of pH on CIP removal by *nat-HA* was investigated at pH levels between 3 and 12. As shown in Figure 5b, CIP elimination increased from 6.6% to 69.6% as the pH rose from 3.0 to 6.0. The observed trend in CIP adsorption can be attributed to the strong electrostatic repulsion between CIP<sup>+</sup> and the positively charged surface of *nat-HA* ( $\equiv P-OH$  and  $\equiv Ca-OH_2^+$ ). For CIP adsorption, pH ranges between 6 and 10.5 were more favorable (close to the  $pH_{PZC}$  value of *nat-HA* where  $\equiv PO^-$  and  $\equiv Ca-OH_2^+$  groups predominate) [46]. Within this pH range, the cationic CIP<sup>+</sup> form transforms into the zwitterionic CIP<sup>±</sup> form. Consequently,  $\equiv PO^-$  and  $\equiv Ca-OH_2^+$  surface sites of *nat-HA* are electrostatically attracted to the  $NH_2^+$  and  $-COO^-$  groups of CIP<sup>±</sup>, respectively. In addition, zwitterionic CIP<sup>±</sup> is more hydrophobic than its cationic and anionic counterparts [15]. Consequently, hydrophobic interactions may play a significant part in the binding interaction of CIP to *nat-HA*. As the pH increased beyond 10.5, the CIP removal effectiveness reduced considerably, possibly due to interactions between the negatively charged functional groups of *nat-HA* ( $\equiv PO^-$  and  $\equiv Ca-OH$ ) and anionic CIP<sup>-</sup>.

### 2.2.2. Effect of the Initial CIP Concentration

In adsorption studies, antibiotic concentration is an important variable to investigate, as most contaminated wastewaters contain varying quantities of pollutants. The initial CIP concentration in the test solution increased from 25 to 200 mg L<sup>-1</sup>, while all other parameters remained constant (pH = 8,  $m = 1 \text{ g L}^{-1}$ ,  $t = 180 \text{ min}$ ,  $T = 298 \text{ K}$ ). The (%) adsorption of CIP decreased from 96.08 to 67.75% from 25 to 200 mg L<sup>-1</sup> (Figure 5c). This absorption at low  $C_0$  can be attributed to the adsorbent's active sites. Nonetheless, a rise in CIP concentration led to a quick saturation of active sites, causing a reduction in removal efficiency.

### 2.2.3. Effect of the Contact Time

Reaction time is another important factor which could significantly influence the adsorption kinetics and capacity. The economic benefits of determining the drug adsorption time in wastewater treatment have been demonstrated. Figure 5d illustrates the influence of contact time on the uptake of CIP onto *nat-HA* sample. All other parameters (pH = 8,  $C_0 = 150 \text{ mg L}^{-1}$ ,  $m = 1 \text{ g L}^{-1}$ , and  $T = 298 \text{ K}$ ) were held constant during the adsorption tests with varying contact times. The kinetics of adsorption can be separated into two phases: rapid and slow; 69.8% of the CIP was adsorbed in the first 25 min; thereafter, the rate slowed until 90 minutes, which coincided with the pseudo-equilibrium time with a 78.5% yield. Then, the adsorption capacities remained practically constant, indicating that a pseudo-equilibrium had been reached between the adsorbent and the adsorbate. For following trials, the optimal contact time was determined to be 90 min. This result may be due to underutilized adsorption sites on the adsorbent's surface. A large number of vacant sites on the *nat-HA* surface was available for adsorption during the initial stage of sorption. As contact duration increases, sorption sites on the surface of the *nat-HA* sample approach saturation. This causes CIP to be transported from the surface of the hydroxyapatite sample into its voids. After a particular period of time, the remaining unoccupied surface sites are occupied and so saturated. The initial high adsorption efficiency is undoubtedly attributable to the large number of available free surface sites, whereas the subsequent slowing is probably due to both a decrease in accessible sites and repulsive interactions between the adsorbed CIP molecules and those in the solution.

#### 2.2.4. Effect of the Adsorbent Dosage

The effect of the adsorbent dosage ( $m$ ) on the CIP removal was evaluated in the range of  $0.25\text{--}3\text{ g L}^{-1}$  adsorbent, maintaining all other variables constant ( $\text{pH} = 8$ ,  $C_0 = 150\text{ mg L}^{-1}$ ,  $t = 90\text{ min}$ ,  $T = 298\text{ K}$ ). As seen in Figure 5e, the CIP removal rate increased with increasing  $m$ , and the maximum  $q_e$  was attained with  $1\text{ g L}^{-1}$  of *nat-HA*. Because of the increase in number of active sites on *nat-HA* samples, CIP removal increased. In the following experiments, a  $1\text{ g L}^{-1}$  adsorbent dosage was therefore considered.

#### 2.3. Adsorption Kinetics

It is essential to examine adsorption kinetics in the treatment of aqueous effluent because it gives significant information about the effectiveness and mechanism of the adsorption process. The pseudo-first-order and pseudo-second-order models [47,48] were applied to the experimental data. The nonlinear forms of pseudo-first and pseudo-second order models are given as follows (3)–(4):

$$\text{Pseudo - first - order : } q_t = q_e \left( 1 - e^{-k_1 t} \right) \quad (3)$$

$$\text{Pseudo - second - order : } q_t = \frac{q_e^2 k_2 t}{1 + q_e k_2 t} \quad (4)$$

where  $k_1$  is the pseudo-first-order adsorption rate constant ( $\text{min}^{-1}$ ),  $q_e$  is the equilibrium adsorption capacity ( $\text{mg g}^{-1}$ ),  $q_t$  is the adsorption capacity at time  $t$  ( $\text{mg g}^{-1}$ ), and  $k_2$  is the pseudo-second-order adsorption rate constant ( $\text{g mg}^{-1} \text{min}^{-1}$ ).

The experimental data of CIP uptake,  $q_t$  vs.  $t$ , were fitted to the models and the results are displayed in Figure 6. Table 1 and Figure 6 present the rate constants. Table 1 reports rate constants ( $k_1$  and  $k_2$ ) and their accompanying regression correlation coefficients ( $R^2$ ). According to the  $R^2$  values (Table 1), the pseudo-second-order kinetic model adequately explained the CIP adsorption, as confirmed by the high level of agreement between the experimental and calculated  $q_e$  values. Thus, the pseudo-second-order model was ideal for modeling the kinetics of CIP adsorption on *nat-HA* [15].

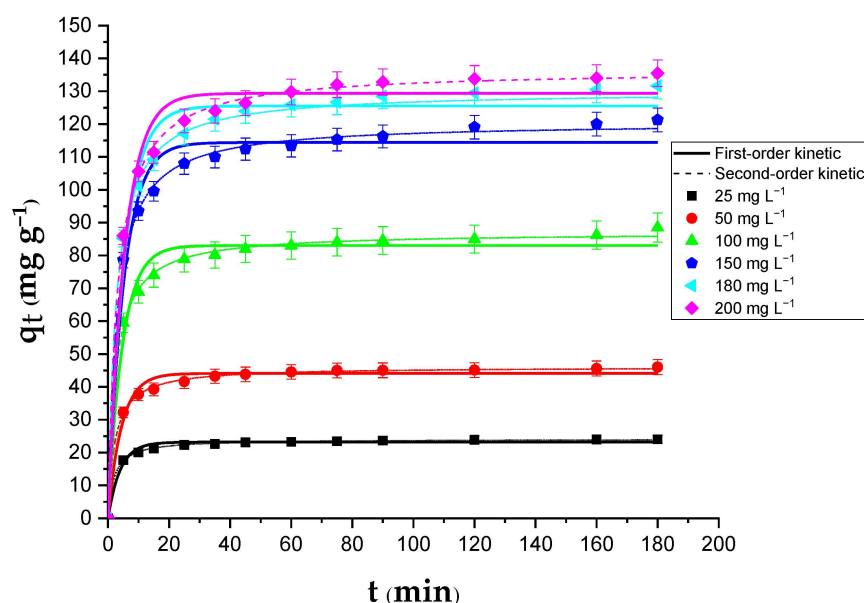


**Figure 6.** Adsorption kinetics (pseudo-first-order and pseudo-second-order kinetic models) of the CIP adsorption onto *nat-HA*.

**Table 1.** Kinetic parameters of CIP adsorption onto *nat*-HA at different initial concentrations.

C <sub>0</sub> (mg L <sup>-1</sup> )	q <sub>e,exp</sub> (mg g <sup>-1</sup> )	Pseudo-First-Order Kinetic Model			Pseudo-Second-Order Kinetic Model		
		k <sub>1</sub> (min <sup>-1</sup> )	q <sub>e,cal</sub> (mg g <sup>-1</sup> )	R <sup>2</sup>	k <sub>2</sub> × 10 <sup>-2</sup> (g mg <sup>-1</sup> min <sup>-1</sup> )	q <sub>e,cal</sub> (mg g <sup>-1</sup> )	R <sup>2</sup>
25	24.00	0.251	23.17	0.984	2.154	24.10	0.999
50	45.05	0.226	44.09	0.981	0.956	46.09	0.999
100	87.35	0.209	82.89	0.973	0.462	87.04	0.998
150	120.00	0.193	114.40	0.976	0.291	120.49	0.998
180	132.65	0.187	125.53	0.978	0.256	132.27	0.999
200	136.00	0.184	129.34	0.978	0.241	136.47	0.999

2.4. Adsorption Isotherms

The data were modeled with the three most common isotherm models, the Langmuir, Freundlich, and Temkin models, to describe the interaction of CIP molecules with the surfaces of *nat*-HA and examine the distribution type of CIP in the liquid and solid phases [49].

The non-linear relationships of those isotherm models can be represented by the expressions reported in Equations (5)–(7) [47,49]:

$$\text{Langmuir isotherm : } q_e = \frac{q_m K_L C_e}{1 + K_L C_e} \tag{5}$$

$$\text{Freundlich isotherm : } q_e = K_F C_e^{1/n_F} \tag{6}$$

$$\text{Temkin isotherm : } q_e = B \ln(A C_e) \tag{7}$$

where q<sub>e</sub> is the equilibrium adsorption capacity (mg g<sup>-1</sup>), q<sub>m</sub> is the maximum adsorption capacity (mg g<sup>-1</sup>), C<sub>e</sub> is the equilibrium CIP concentration (mg L<sup>-1</sup>), K<sub>L</sub> is the Langmuir constant (mg L<sup>-1</sup>), K<sub>F</sub> is the Freundlich adsorbent capacity, n<sub>F</sub> is the heterogeneity factor, B (mg g<sup>-1</sup>) is the Temkin constant, and A is the Temkin equilibrium binding constant (L mg<sup>-1</sup>).

Figure 7 shows the plots of these isotherm models, and Table 2 lists all of their coefficients.

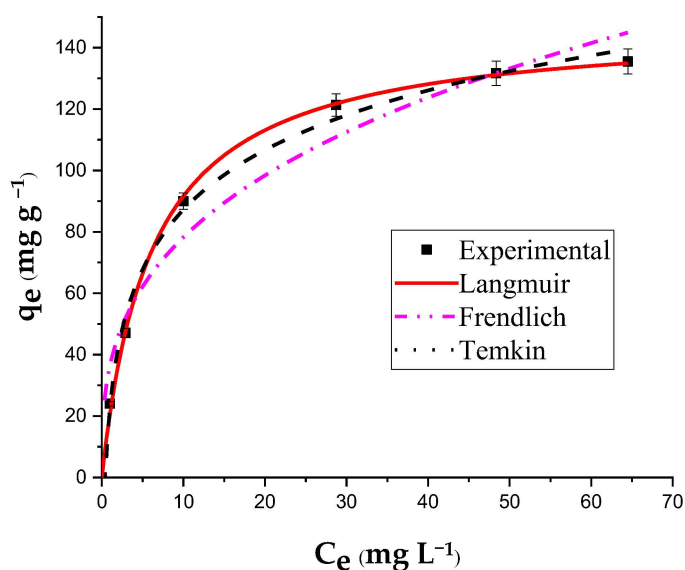


**Figure 7.** Langmuir, Freundlich, and Temkin models’ fitting of CIP adsorption isotherms on *nat*-HA.

**Table 2.** Isotherm parameters of CIP adsorption on *nat-HA*.

Isotherm	Parameters	Values
Langmuir	$q_m$ (mg g <sup>-1</sup> )	147.70
	$K_L$ (L mg <sup>-1</sup> )	0.163
	$R^2$	0.999
	$R_L$	0.197
Freundlich	$K_F$	36.50
	$N$	3.02
	$R^2$	0.954
Temkin	$A$ (L mg <sup>-1</sup> )	2.25
	$B$ (mg g <sup>-1</sup> )	28.0
	$R^2$	0.996

The Langmuir isotherm can be defined in terms of the dimensionless constant separation factor,  $R_L$ , as demonstrated by the following Equation (8):

$$R_L = \frac{1}{1 + K_L C_0} \quad (8)$$

The  $R_L$  parameter is thought to be a more trustworthy indicator of adsorption [47,50]. This determines whether the form of the isotherm is unfavorable ( $R_L > 1$ ), linear ( $R_L = 1$ ), favorable ( $0 < R_L < 1$ ), or irreversible ( $R_L = 0$ ).

The Langmuir adsorption isotherm model fit the experimental data best, with the highest regression coefficient ( $R^2 = 0.999$ ) compared to other isotherm models; it indicated that adsorption was relatively high ( $q_m = 147.7$  mg g<sup>-1</sup>). These data suggest that the adsorption of CIP onto the surface of *nat-HA* is due to monolayer adsorption. The  $R_L$  value of 0.197 indicates a favorable adsorption process. The Temkin adsorption potential ( $B \ln A$ ) was 22.68 kJ mol<sup>-1</sup>, indicating that the binding between CIP molecules and *nat-HA* was quite weak. The Temkin model's high correlation coefficient ( $R^2 = 0.996$ ) indicated good linearity.

### 2.5. Thermodynamic Study

The adsorption process can be characterized by thermodynamic parameters, such as Gibbs free energy change ( $\Delta G^\circ$ ), enthalpy change ( $\Delta H^\circ$ ), and entropy change ( $\Delta S^\circ$ ). The  $\Delta G^\circ$  of adsorption is calculated as follows (9):

$$\Delta G^\circ = -RT \ln K_L^\circ \quad (9)$$

where  $R$  represents the universal gas constant (8.314 J mol<sup>-1</sup>K<sup>-1</sup>),  $T$  represents the temperature (K), and  $K_L^\circ$  is the "thermodynamic" Langmuir constant for the adsorption process (dimensionless). To obtain this value from the Langmuir Equation (5),  $K_L$  (L mg<sup>-1</sup>), all concentrations must be converted to the molar form and the standard state temperature must be accounted for 1 mol L<sup>-1</sup> as follows (10) [51,52]:

$$K_L^\circ = K_L \text{ (L mg}^{-1}\text{)} \times 1000 \text{ (mg g}^{-1}\text{)} \times M \text{ (g mol}^{-1}\text{)} \times C^\circ \text{ (mol L}^{-1}\text{)} \quad (10)$$

where  $M = 331.4$  g mol<sup>-1</sup> is the molar mass of CIP. The classical relationships were used to determine the  $\Delta H^\circ$  and  $\Delta S^\circ$  parameters as follows (11)–(12):

$$\ln K_L^\circ = (\Delta S^\circ/R) - (\Delta H^\circ/RT) \quad (11)$$

$$\Delta G^\circ = \Delta H^\circ - T\Delta S^\circ \quad (12)$$

The plot of  $\ln K_L^\circ$  vs.  $1/T$  (not shown) resulted in a straight line, and from the intercept and slope of these Van 't Hoff plots, the values of  $\Delta H^\circ$  (kJ mol<sup>-1</sup>) and  $\Delta S^\circ$

( $\text{J mol}^{-1}\text{K}^{-1}$ ) may be derived, respectively;  $\Delta G^\circ$  values ( $\text{kJ mol}^{-1}$ ) were computed using the  $\Delta H^\circ$  and  $\Delta S^\circ$  measurements.

Table 3 displays the thermodynamic values calculated for  $C_0 = 150 \text{ mg L}^{-1}$  and  $m = 1 \text{ g L}^{-1}$  at a pH of 8.

**Table 3.** Thermodynamic parameters for adsorption of CIP onto *nat-HA*.

T (K)	$K_L$ ( $\text{L mg}^{-1}$ )	$K_L^\circ (\times 10^5)$ (Dimensionless)	$\text{Ln } K_L^\circ$	$\Delta G^\circ$ ( $\text{kJ mol}^{-1}$ )	$\Delta H^\circ$ ( $\text{kJ mol}^{-1}$ )	$\Delta S^\circ$ ( $\text{J mol}^{-1}\text{K}^{-1}$ )
298	0.1004	3.3272	10.41	−25.77	−21.09	15.72
308	0.0742	2.4589	10.11	−25.93		
318	0.0588	1.9486	9.87	−26.09		
328	0.0457	1.5144	9.62	−26.24		

The negative value of  $\Delta H^\circ$  confirmed the exothermic adsorption of CIP on *nat-HA*; the  $\Delta H^\circ$  is  $<40 \text{ kJ mol}^{-1}$ , indicating that the interaction between CIP and *nat-HA* is weak (physisorption) [52]. This is consistent with the suggested adsorption mechanism. During the adsorption process, the positive value of  $\Delta S^\circ$  ( $15.72 \text{ J mol}^{-1}\text{K}^{-1}$ ) showed an increase in disorder at the solution/*nat-HA* interphase, corresponded to an increase in randomness at the solid–solute interface, and implied that CIP has a strong affinity for *nat-HA*. Similarly significant results were also reported in [47,53]. The value of  $\Delta G^\circ$  was negative at all the temperatures investigated, indicating that the adsorption of CIP onto *nat-HA* occurred spontaneously [54]. In addition, the increase in the negative value of  $\Delta G^\circ$  with temperature showed that the removal process was more advantageous at lower temperatures.

## 2.6. Photodegradation of CIP on $\text{TiO}_2$

As noted in the introduction, adsorption considerably reduces antibiotic concentrations, but not enough to meet water quality criteria. To this end,  $\text{TiO}_2$  PC500 was used as a photocatalyst; with a band gap of  $\sim 3.2 \text{ eV}$ ,  $\text{TiO}_2$  was activated under ultraviolet light (9 W Philips lamp). To estimate the efficacy of photodegradation of CIP on  $\text{TiO}_2$ , it is necessary to investigate the fluctuation of two crucial parameters such as the catalyst dose and the pollutant concentration ( $C_{0r}$ ).

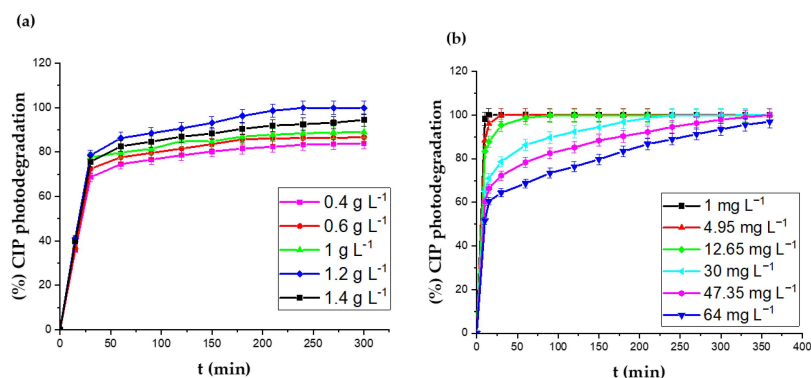
### 2.6.1. Effect of the Catalyst Dose

Figure 8a illustrates the photodegradation rate of CIP ( $C_{0r} = 30 \text{ mg L}^{-1}$ ) in the presence of various dosages of  $\text{TiO}_2$  ( $0.4\text{--}1.4 \text{ g L}^{-1}$ ). When the photocatalyst dose was increased from  $0.4$  to  $1.2 \text{ g L}^{-1}$ , the photodegradation efficiency of CIP increased from 84 to  $\sim 100\%$ . Subsequently, a minor decline was noticed when an additional catalyst was introduced. This is because the number of photoactive sites for CIP oxidation increased, and the photocatalytic activity increased at  $1.2 \text{ g L}^{-1}$ . The decrease in photoactivity was due to the opacity of the suspension, turbidity, and light scattering of the catalyst particles. The shadowing effect and the blocking and dispersion of incident light by excess  $\text{TiO}_2$  particles also contribute to the decreased performance [36]. All of these conditions would reduce the UV light intensity on the surface of the catalyst, hence decreasing the photodegradation efficiency.

### 2.6.2. Effect of the Initial CIP Concentration

The influence of the initial concentration on photodegradation and mineralization was investigated with a fixed dose of  $\text{TiO}_2$  ( $1 \text{ g L}^{-1}$ ) at room temperature and pH  $\sim 5$  utilizing the residual concentrations after CIP adsorption  $C_{0r}$  ( $1, 4.95, 12.65, 30, 47.35,$  and  $64.00 \text{ mg L}^{-1}$ ). The acquired data validated the observed trend of pollutant degradation (Figures 8b and 9). Notably, as the initial CIP concentration increased, both the degradation efficiency and mineralization decreased. The highest degradation efficiency and mineralization yield were  $\sim 100\%$  and  $98.5\%$ , respectively, for  $1 \text{ mg L}^{-1}$  initial CIP. This can be explained by the fact that as the initial concentration of CIP increases, more molecules are adsorbed onto the photocatalyst surface. Therefore, the adsorption of  $\text{O}_2^{\bullet-}$  and  $\text{OH}^\bullet$ ,

which are responsible for the advanced oxidation process (AOP), is lowered on the photocatalyst. In addition, photons are prevented from reaching the photocatalyst surface and are therefore not absorbed. Consequently, elimination rates are diminished at high initial CIP concentrations [55,56]. Mineralization appears to be more responsive to variations in CIP concentration than CIP degradation. For instance, the 360 min TOC reduction is 21%, 34.5%, 42.6%, 70.5%, 82.3%, and 98.5% at 64, 47.35, 30, 12.65, 4.95, and 1 mg L<sup>-1</sup> CIP, respectively. Mineralization involves a series of processes including the oxidation of CIP photocatalytic transformation byproducts to CO<sub>2</sub> and water, which is less likely to occur than the partial oxidation of CIP [57–63].



**Figure 8.** Physical parameters influencing CIP photodegradation on TiO<sub>2</sub>: (a) catalyst dose and (b) initial concentration (C<sub>0r</sub>) of CIP.

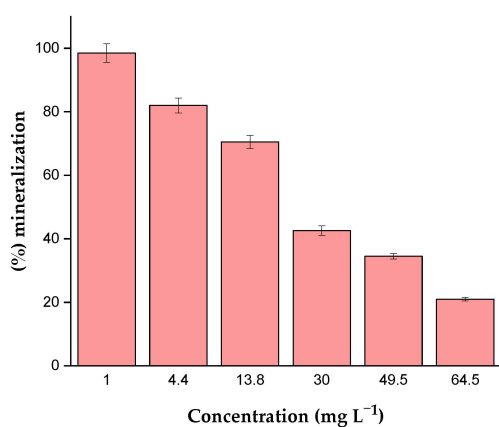
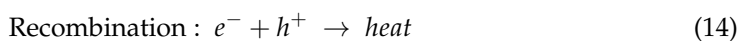
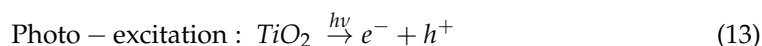


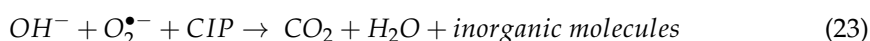
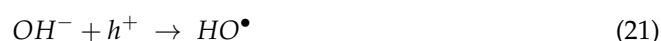
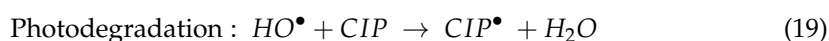
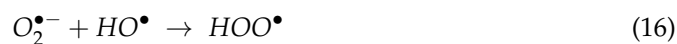
**Figure 9.** Mineralization yield versus CIP concentration after 360 min UV irradiation.

### 2.6.3. Proposed Transformation Scheme of CIP Photodegradation

The photocatalytic mechanism of TiO<sub>2</sub> is activated by the absorption of photon  $h\nu$  with energy equal to or greater than the band gap of TiO<sub>2</sub>. This produces an electron-hole pair on the surface of the TiO<sub>2</sub> nanoparticle [57].

The proposed transformation scheme for the degradation of CIP over TiO<sub>2</sub> under UV light can be summarized as follows (13)–(23):





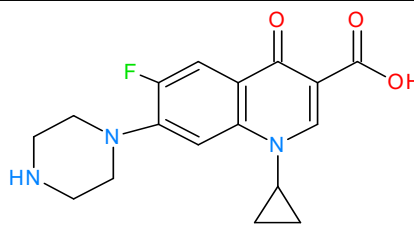
When photocatalysts absorb a photon with an energy greater than or equal to the band gap between the conduction band (CB) and the valence band (VB), an electron is promoted to the CB and a positive hole (represented by  $h^+$ ) is created in the VB. Electrons and holes that are excited can recombine and release their energy as heat, or they can become trapped in metastable surface states. In addition, they can also interact with electron donors and acceptors that have been adsorbed on the surface or in the electrical double layer of charged particles that surrounds them. Redox reactions initiated by these electron donors and acceptors could generate reactive oxygen species, including hydroxyl ( $OH^{\bullet}$ ) radicals and superoxide radical anions ( $O_2^{\bullet-}$ ). Depending on the specific conditions, these species are the main contributors towards the oxidation of organic contaminants and are significant in the photocatalytic reaction mechanism of CIP [58,59].

### 3. Materials and Methods

#### 3.1. Chemicals and Materials

CIP was purchased from Sigma-Aldrich Chemical Company (Shanghai, China). The structure and the relevant physicochemical properties of CIP are shown in Table 4. Using  $0.1 \text{ mol L}^{-1}$  NaOH and  $0.1 \text{ mol L}^{-1}$  HCl, pH was adjusted. In the photocatalytic experiment,  $TiO_2$  Millennium PC500 (anatase, Sigma-Aldrich Chemical Company (Shanghai, China)) was utilized. All solutions were prepared using ultrapure water (ADRONA SIA Process and Laboratory Systems, Riga, Latvia) (Adrona, Millipore Milli-Q UV Plus, R = 18.25 M $\Omega$ ).

**Table 4.** Chemical structure and physicochemical properties of CIP.

Molecular formula	$C_{17}H_{18}O_3N_3F$
Purity	$\geq 98\%$
Molecular weight	$331.4 \text{ g mol}^{-1}$
pKa	$pK_{a1} = 6.1$ [60] $pK_{a2} = 8.9$ [60]
Chemical structure	

### 3.2. Preparation of nat-HA

The sample of natural hydroxyapatite (*nat-HA*) used in this research was produced as follows. The cortical bone of mature bovines (2–3 years old) was procured from a Bouira slaughterhouse (Algeria) and washed to remove visible tissues and compounds from the surface of the bone. The material was then sliced into rectangular samples. The as-received bone samples were treated in an electric furnace (Nabertherm GmbH Lilienthal, Germany) at a temperature of 800 °C, with a heating/cooling rate of 5 °C/min and a holding time of 3 h. The sintered product was ground with a mortar and pestle and sieved through a No. 100 mesh screen.

### 3.3. Characterization of nat-HA

The *nat-HA* XRD pattern was acquired and recorded on a D8 Advance Bruker X-ray diffractometer (Karlsruhe, Germany) using Cu K $\alpha$  radiation at a 2 $\theta$  angle ranging from 20° to 50°. With the aid of JCPDS files, the phases were identified. Fourier-transform infrared (FT-IR) spectra were recorded on a Perkin Elmer FT-IR-300 spectrometer (Japan) using the KBr pellet technique with a scan range of 400–4000 cm<sup>-1</sup>. The morphology of the powder was examined with scanning electron microscopy SEM, Philips XL 30 (Eindhoven, The Netherlands). In order to better understand the adsorption mechanism of the CIP antibiotic, the point of zero charge (pH<sub>PZC</sub>) of natural hydroxyapatite was determined [61].

### 3.4. Batch Adsorption and Photoactivity

#### 3.4.1. Adsorption Study

Adsorption studies were carried out in the batch mode using 200 mL conical flasks containing a total of 100 mL of the ciprofloxacin antibiotic under pH 5 for 3 h, adding HCl or NaOH to adjust the pH of the working solution to the desired level. The solution was agitated at 300 rpm at 303 K to achieve the adsorption/desorption equilibrium. The samples were then retrieved at suitable intervals and centrifuged for 15 minutes at 3500 rpm. The residual CIP concentration was determined using a UV-Vis spectrophotometer (Agilent Technologies Cary 60 UV-Vis, Santa Clara, CA, USA) at fixed wavelength 275 nm. The influence of some key operational parameters including initial pH (3–12), C<sub>0</sub> (25–200 mg L<sup>-1</sup>), *t* (1–200 min), and *m* (0.25–3 g L<sup>-1</sup>) on the CIP adsorption capacity were studied. Under the identical conditions, each experiment was run in triplicate. The adsorption capacity (*q<sub>t</sub>*) and the removal percentage (% *adsorption*) of CIP by *nat-HA* were calculated at any time (*t*) using the following mass balance Equations (24) and (25):

$$q_t = \left( \frac{C_0 - C_t}{m} \right) \times V \quad (24)$$

$$(\%)adsorption = \left( \frac{C_0 - C_t}{C_0} \right) \times 100 \quad (25)$$

where C<sub>0</sub> and C<sub>*t*</sub> (mg L<sup>-1</sup>) are the CIP concentrations at time zero and time *t*, respectively, V (L) represents the volume of the solution, whereas *m* (g) represents the quantity of the *nat-HA* adsorbent employed.

#### 3.4.2. Photocatalytic Experiments

The photocatalytic experiments for the remaining concentrations were carried out in a Pyrex vessel (7.5 cm height × 6 cm diameter) encircled by a thermostatically controlled water circulation system (25 ± 0.3 °C). One hundred milliliters of the remaining CIP solution and 1 g L<sup>-1</sup> of the TiO<sub>2</sub> PC500 photocatalyst were put into the reactor, and the solution was constantly stirred using a magnetic stirrer (200 rpm). Blank experiments were conducted under the dark condition and evidenced no CIP adsorption for 30 min. A UV lamp Philips PL-S 9W/10/2P (Amsterdam, The Netherlands) was placed inside of the cover. Before analysis, 2 mL of the aliquot were retrieved at various time intervals (1–360 min) and the solid was separated from the solution by filtration with PTFE Millipore (0.45 μm)

syringe filters (Bedford, MA, USA). Under the identical conditions, each experiment was run in triplicate.

The photodegradation efficiency of CIP was calculated by applying the following Formula (26):

$$(\%) \text{ degradation} = \left( \frac{C_{0r} - C_t}{C_{0r}} \right) \times 100 \quad (26)$$

where  $C_{0r}$  and  $C_t$  are the remaining CIP concentration and its residual concentration at time  $t$ , respectively.

The Total Organic Carbon (TOC) was measured with a TOC analyzer (Shimadzu TOCVCSH) (Shimadzu TOC-VCSH, Japan), and the yield was obtained using the following Formula (27):

$$(\%) \text{ mineralization} = \left( \frac{TOC_0 - TOC_t}{TOC_0} \right) \times 100 \quad (27)$$

where  $TOC_0$  and  $TOC_t$  are the initial total organic carbon and the total organic carbon at time  $t$ , respectively.

#### 4. Conclusions

The *nat-HA* employed in this study exhibited a better adsorption capacity for CIP. The Langmuir model was demonstrated to accurately fit the adsorption isotherm, indicating that adsorption happens via monolayer coverage. According to the kinetic calculations, adsorption followed the pseudo-second-order model. Adsorption is exothermic, as indicated by the negative enthalpy changes during the adsorption process. The increase in CIP concentration increased the adsorption capacity but decreased the adsorption kinetics. The value of  $\Delta H^\circ$  was  $<40 \text{ kJ mol}^{-1}$ , showing that weak bonds (physisorption) were formed between CIP and *nat-HA*. This proposal was consistent with the hypothesized mechanism for adsorption. The positive value of  $\Delta S^\circ$  corresponded to an increase in the randomness at the solid–solute interface. The photodegradation of the remaining concentrations of CIP on  $\text{TiO}_2$  under UV light resulted in a considerable increase in the elimination efficiency of the free radicals  $\text{O}_2^{\bullet-}$  and  $\text{OH}^\bullet$  via the conduction and valence bands, respectively. The increase in the  $\text{TiO}_2$  dosage decreased the removal efficiency owing to the decrease in the UV intensity reaching the surface. It was demonstrated that natural hydroxyapatite could be used for pharmaceutical industrial effluent treatment.

**Author Contributions:** Conceptualization, S.C., A.I., A.H. and L.M.; methodology, S.C., A.I., A.H., A.A. (Aymen Assadi) and L.M.; validation, J.-C.B., A.B., A.A. (Aymen Assadi), A.A. (Abdeltif Amrane) and L.M.; formal analysis, J.-C.B., A.B., A.A. (Aymen Assadi) and A.M.; investigation, S.C.; resources, L.M., A.I., A.E.J. and A.M.; data curation, S.C., A.I., A.H. and L.M.; writing—original draft preparation, S.C. and A.I.; writing—review and editing, S.C., A.I., A.H., L.M., A.A. (Abdeltif Amrane) and J.-C.B.; visualization, S.C., L.M., J.-C.B., M.Z. and A.A. (Aymen Assadi); supervision, L.M., A.A. (Abdeltif Amrane) and J.-C.B.; project administration, L.M. and A.A. (Aymen Assadi). All authors have read and agreed to the published version of the manuscript.

**Funding:** This research received no external funding.

**Data Availability Statement:** Not applicable.

**Acknowledgments:** This work was supported by the King Khalid University, Abha, Saudi Arabia. The authors extend their appreciation to the Deanship of Scientific Research at King Khalid University for funding this work through Larg Groups Project under grant number (R.G.P. 2/37/43).

**Conflicts of Interest:** The authors declare no conflict of interest.

## References

1. Fobbe, R.; Kuhlmann, B.; Nolte, J.; Preuß, G.; Skark, C.; Zullei-Seibert, N. Organic Pollutants in the Water Cycle: Properties, Occurrence, Analysis and Environmental Relevance of Polar Compounds. In *Organic Pollutants in the Water Cycle: Properties, Occurrence, Analysis and Environmental Relevance of Polar Compounds*; Wiley: Hoboken, NJ, USA, 2006; pp. 121–153. ISBN 978-3-527-60877-5.
2. Halling-Sørensen, B.; Lützhøft, H.-C.; Andersen, H.; Ingerslev, F. Environmental Risk Assessment of Antibiotics: Comparison of Mecillinam, Trimethoprim and Ciprofloxacin. *J. Antimicrob. Chemother.* **2000**, *46*, 53–58. [[CrossRef](#)] [[PubMed](#)]
3. Kümmerer, K. The Presence of Pharmaceuticals in the Environment Due to Human Use—Present Knowledge and Future Challenges. *J. Environ. Manag.* **2009**, *90*, 2354–2366. [[CrossRef](#)] [[PubMed](#)]
4. Jalil, M.; Baschini, M.; Sapag, K. Removal of Ciprofloxacin from Aqueous Solutions Using Pillared Clays. *Materials* **2017**, *10*, 1345. [[CrossRef](#)] [[PubMed](#)]
5. Wang, C.-J.; Li, Z.; Jiang, W.-T. Adsorption of Ciprofloxacin on 2:1 Dioctahedral Clay Minerals. *Appl. Clay Sci.* **2011**, *53*, 723–728. [[CrossRef](#)]
6. Hu, D.; Wang, L. Adsorption of Ciprofloxacin from Aqueous Solutions onto Cationic and Anionic Flax Noil Cellulose. *Desalin. Water Treat.* **2016**, *57*, 1–14. [[CrossRef](#)]
7. Jiang, W.-T.; Chang, P.-H.; Wang, Y.-S.; Yolin, T.; Jean, J.-S.; Li, Z.; Krukowski, K. Removal of Ciprofloxacin from Water by Birnessite. *J. Hazard. Mater.* **2013**, *250–251*, 362–369. [[CrossRef](#)]
8. Sun, Y.; Yue, Q.; Gao, B.; Gao, Y.; Xu, X.; Li, Q.; Wang, Y. Adsorption and Cosorption of Ciprofloxacin and Ni(II) on Activated Carbon—Mechanism Study. *J. Taiwan Inst. Chem. Eng.* **2014**, *45*, 681–688. [[CrossRef](#)]
9. Peng, X.; Hu, F.; Huang, J.; Wang, Y.; Dai, H.; Liu, Z. Preparation of a Graphitic Ordered Mesoporous Carbon and Its Application in Sorption of Ciprofloxacin: Kinetics, Isotherm, Adsorption Mechanisms Studies. *Microporous Mesoporous Mater.* **2016**, *228*, 196–206. [[CrossRef](#)]
10. Mao, H.; Wang, S.; Lin, J.-Y.; Wang, Z.; Ren, J. Modification of a Magnetic Carbon Composite for Ciprofloxacin Adsorption. *J. Environ. Sci.* **2016**, *49*, 179–188. [[CrossRef](#)]
11. Liang, C.; Zhang, X.; Feng, P.; Chai, H.; Huang, Y. ZIF-67 Derived Hollow Cobalt Sulfide as Superior Adsorbent for Effective Adsorption Removal of Ciprofloxacin Antibiotics. *Chem. Eng. J.* **2018**, *344*, 95–104. [[CrossRef](#)]
12. Reymann, T.; Kerner, M.; Kümmerer, K. Assessment of the Biotic and Abiotic Elimination Processes of Five Micropollutants during Cultivation of the Green Microalgae *Acutodesmus Obliquus*. *Bioresour. Technol. Rep.* **2020**, *11*, 100512. [[CrossRef](#)]
13. Gil, M.; Alvarez, S.; Peres, J.; Ovejero, G. Effective Adsorption of Non-Biodegradable Pharmaceuticals from Hospital Wastewater with Different Carbon Materials. *Chem. Eng. J.* **2017**, *320*, 319. [[CrossRef](#)]
14. Gouza, A.; Saoiabi, S.; el Karbane, M.; Masse, S.; Laurent, G.; Rami, A.; Saoiabi, A.; Laghzizil, A.; Coradin, T. Oil Shale Powders and Their Interactions with Ciprofloxacin, Ofloxacin, and Oxytetracycline Antibiotics. *Environ. Sci. Pollut. Res.* **2017**, *24*, 25977–25985. [[CrossRef](#)]
15. Laabd, M.; Brahmi, Y.; El Ibrahim, B.; Hsini, A.; Toufik, E.M.; Abdellaoui, Y.; Abou Oualid, H.; Ouardi, M.; Albourine, A. A Novel Mesoporous Hydroxyapatite@Montmorillonite Hybrid Composite for High-Performance Removal of Emerging Ciprofloxacin Antibiotic from Water: Integrated Experimental and Monte Carlo Computational Assessment. *J. Mol. Liq.* **2021**, *338*, 116705. [[CrossRef](#)]
16. Xiao, X.; Zeng, X.; Lemley, A. Species-Dependent Degradation of Ciprofloxacin in a Membrane Anodic Fenton System. *J. Agric. Food Chem.* **2010**, *58*, 10169–10175. [[CrossRef](#)]
17. Xiao, X.; Sun, S.-P.; McBride, M.; Lemley, A. Degradation of Ciprofloxacin by Cryptomelane-Type Manganese(III/IV) Oxides. *Environ. Sci. Pollut. Res. Int.* **2012**, *20*, 10–21. [[CrossRef](#)]
18. Li, B.; Zhang, T. PH Significantly Affects Removal of Trace Antibiotics in Chlorination of Municipal Wastewater. *Water Res.* **2012**, *46*, 3703–3713. [[CrossRef](#)]
19. Nasuhoglu, D.; Rodayan, A.; Berk, D.; Yargeau, V. Removal of the Antibiotic Levofloxacin (LEVO) in Water by Ozonation and TiO<sub>2</sub> Photocatalysis. *Chem. Eng. J.* **2012**, *189–190*, 41–48. [[CrossRef](#)]
20. Li, W.; Su, B.; Xu, J. Photodegradation of Four Fluoroquinolone Compounds by Titanium Dioxide under Simulated Solar Light Irradiation. *J. Chem. Technol. Biotechnol.* **2012**, *87*, 643–650. [[CrossRef](#)]
21. Vasquez, M.; Hapeshi, E.; Fatta-Kassinos, D.; Kümmerer, K. Biodegradation Potential of Ofloxacin and Its Resulting Transformation Products during Photolytic and Photocatalytic Treatment. *Environ. Sci. Pollut. Res. Int.* **2012**, *20*, 1302–1309. [[CrossRef](#)]
22. Li, B.; Zhang, T. Biodegradation and Adsorption of Antibiotics in the Activated Sludge Process. *Environ. Sci. Technol.* **2010**, *44*, 3468–3473. [[CrossRef](#)] [[PubMed](#)]
23. Dorival García, N.; Zafra Gomez, A.; Navalón, A.; González, J.; Vílchez, J. Removal of Quinolone Antibiotics from Wastewaters by Sorption and Biological Degradation in Laboratory-Scale Membrane Bioreactors. *Sci. Total Environ.* **2012**, *442C*, 317–328. [[CrossRef](#)] [[PubMed](#)]
24. Genç, N.; Can, E. Adsorption Kinetics of the Antibiotic Ciprofloxacin on Bentonite, Activated Carbon, Zeolite, and Pumice. *Desalin. Water Treat.* **2015**, *53*, 785–793. [[CrossRef](#)]
25. Chen, Y.; Lan, T.; Duan, L.; Wang, F.; Zhao, B.; Zhang, S.; Wei, W. Adsorptive Removal and Adsorption Kinetics of Fluoroquinolone by Nano-Hydroxyapatite. *PLoS ONE* **2015**, *10*, e0145025. [[CrossRef](#)]

26. Haciosmanoğlu, G.G.; Mejías, C.; Martín Bueno, J.; Santos, J.; Aparicio, I.; Alonso, E. Antibiotic Adsorption by Natural and Modified Clay Minerals as Designer Adsorbents for Wastewater Treatment: A Comprehensive Review. *J. Environ. Manag.* **2022**, *317*, 115397. [[CrossRef](#)]
27. Li, M.; Liu, Y.; Zeng, G.; Liu, N.; Liu, S. Graphene and Graphene-Based Nanocomposites Used for Antibiotics Removal in Water Treatment: A Review. *Chemosphere* **2019**, *226*, 360–380. [[CrossRef](#)]
28. Khanday, W.; Ahmed, M.; Okoye, U.; Hummadi, E.; Hameed, B. Single-Step Pyrolysis of Phosphoric Acid-Activated Chitin for Efficient Adsorption of Cephalexin Antibiotic. *Bioresour. Technol.* **2019**, *280*, 255–259. [[CrossRef](#)]
29. Magesh, N.; Renita, A.; Ponnusamy, S.K. Practice on Treating Pharmaceutical Compounds (Antibiotics) Present in Waste Water Using Biosorption Technique with Different Bio Waste Compounds. A Review. *Environ. Prog. Sustain. Energy* **2020**, *39*, e13429. [[CrossRef](#)]
30. Benedini, L.; Placente, D.; Ruso, J.; Messina, P. Adsorption/Desorption Study of Antibiotic and Anti-Inflammatory Drugs onto Bioactive Hydroxyapatite Nano-Rods. *Mater. Sci. Eng. C* **2019**, *99*, 180–190. [[CrossRef](#)]
31. Ragab, A.; Ahmed, I.; Bader, D. The Removal of Brilliant Green Dye from Aqueous Solution Using Nano Hydroxyapatite/Chitosan Composite as a Sorbent. *Molecules* **2019**, *24*, 847. [[CrossRef](#)]
32. Uddin, M.J.; Ampiauw, R.; Lee, W. Adsorptive Removal of Dyes from Wastewater Using a Metal-Organic Framework: A Review. *Chemosphere* **2021**, *284*, 131314. [[CrossRef](#)]
33. Mondal, S.; Dorozhkin, S.; Pal, U. Recent Progress on Fabrication and Drug Delivery Applications of Nanostructured Hydroxyapatite. *Wiley Interdiscip. Rev. Nanomed. Nanobiotechnol.* **2017**, *10*, e1504. [[CrossRef](#)]
34. Pai, S.; Kini, S.; Selvaraj, R.; Pugazhendhi, A. A Review on the Synthesis of Hydroxyapatite, Its Composites and Adsorptive Removal of Pollutants from Wastewater. *J. Water Process Eng.* **2020**, *38*, 101574. [[CrossRef](#)]
35. Xia, Z.; Yu, X.; Jiang, X.; Brody, H.; Rowe, D.; Wei, M. Fabrication and Characterization of Biomimetic Collagen-Apatite Scaffolds with Tunable Structures for Bone Tissue Engineering. *Acta Biomater.* **2013**, *9*, 7308–7319. [[CrossRef](#)]
36. Mekatel, E.H.; Samira, A.; Bellal, B.; Trari, M.; Djamel, N. Photocatalytic Reduction of Cr(VI) on Nanosized Fe<sub>2</sub>O<sub>3</sub> Supported on Natural Algerian Clay: Characteristics, Kinetic and Thermodynamic Study. *Chem. Eng. J.* **2012**, *200–202*, 611–618. [[CrossRef](#)]
37. Belbachir, I.; Makhoukhi, B. Adsorption of Bezathren Dyes onto Sodic Bentonite from Aqueous Solutions. *J. Taiwan Inst. Chem. Eng.* **2017**, *75*, 105–111. [[CrossRef](#)]
38. Chong, M.N.; Jin, B.; Chow, C.; Saint, C. Recent Developments in Photocatalytic Water Treatment Technology: A Review. *Water Res.* **2010**, *44*, 2997–3027. [[CrossRef](#)]
39. Çalışkan, Y.; Yatmaz, H.; Bektaş, N. Photocatalytic Oxidation of High Concentrated Dye Solutions Enhanced by Hydrodynamic Cavitation in a Pilot Reactor. *Process Saf. Environ. Prot.* **2017**, *111*, 428–438. [[CrossRef](#)]
40. Mekatel, E.H.; Samira, A.; Trari, M.; Djamel, N.; Dahdouh, N.; Ladjali, S. Combined Adsorption/Photocatalysis Process for the Decolorization of Acid Orange 61. *Arab. J. Sci. Eng.* **2018**, *44*, 5311–5322. [[CrossRef](#)]
41. Silva, T.; Silva, M.; Cunha-Queda, C.; Fonseca, A.; Saraiva, I.; Boaventura, R.; Vilar, V. Sanitary Landfill Leachate Treatment Using Combined Solar Photo-Fenton and Biological Oxidation Processes at Pre-Industrial Scale. *Chem. Eng. J.* **2013**, *228*, 850–866. [[CrossRef](#)]
42. Ooi, C.Y.; Abd Shukor, M.; Singh, R. Properties of Hydroxyapatite Produced by Annealing of Bovine Bone. *Ceram. Int.* **2007**, *33*, 1171–1177. [[CrossRef](#)]
43. Wang, X.; Wang, Z.; Fan, H.; Xiao, Y.; Zhang, X. Fabrication of Porous Hydroxyapatite Ceramics by Microwave Sintering Method. *Key Eng. Mater.* **2005**, *288–289*, 529–532. [[CrossRef](#)]
44. Harja, M.; Ciobanu, G. Studies on Adsorption of Oxytetracycline from Aqueous Solutions onto Hydroxyapatite. *Sci. Total Environ.* **2018**, *628–629*, 36–43. [[CrossRef](#)] [[PubMed](#)]
45. Agougui, H.; Jabli, M.; Majdoub, H. Synthesis, Characterization of Hydroxyapatite-Lambda Carrageenan and Evaluation of Its Performance for the Adsorption of Methylene Blue from Aqueous Suspension. *J. Appl. Polym. Sci.* **2017**, *134*, 45385. [[CrossRef](#)]
46. Yuan, L.; Yan, M.; Huang, Z.; He, K.; Zeng, G.; Chen, A.; Hu, L.; Hui, L.; Peng, M.; Huang, T.; et al. Influences of PH and Metal Ions on the Interactions of Oxytetracycline onto Nano-Hydroxyapatite and Their Co-Adsorption Behavior in Aqueous Solution. *J. Colloid Interface Sci.* **2019**, *541*, 101–113. [[CrossRef](#)]
47. Sapawe, N.; Abdul Jalil, A.; Triwahyono, S.; Shah, M.; Jusoh, R.; Salleh, N.F.; Hameed, B.; Karim, A.; Bahru, J.; Malaysia, J. Cost-Effective Microwave Rapid Synthesis of Zeolite NaA for Removal of Methylene Blue. *Chem. Eng. J.* **2013**, *229*, 388–398. [[CrossRef](#)]
48. Hameed, B. Removal of Cationic Dye from Aqueous Solution Using Jackfruit Peel as Non-Conventional Low-Cost Adsorbent. *J. Hazard. Mater.* **2008**, *162*, 344–350. [[CrossRef](#)]
49. Auta, M.; Hameed, B. Modified Mesoporous Clay Adsorbent for Adsorption Isotherm and Kinetics of Methylene Blue. *Chem. Eng. J.* **2012**, *198–199*, 219–227. [[CrossRef](#)]
50. Mouni, L.; Belkhir, L.; Bollinger, J.-C.; Bouzaza, A.; Tiri, A.; Dahmoune, F.; Madani, K.; Remini, H. Removal of Methylene Blue from Aqueous Solutions by Adsorption on Kaolin: Kinetic and Equilibrium Studies. *Appl. Clay Sci.* **2018**, *153*, 38–45. [[CrossRef](#)]
51. Salvestrini, S.; Leone, V.; Iovino, P.; Canzano, S.; Capasso, S. Considerations about the Correct Evaluation of Sorption Thermodynamic Parameters from Equilibrium Isotherms. *J. Chem. Thermodyn.* **2014**, *68*, 310–316. [[CrossRef](#)]

52. Imessaoudene, A.; Cheikh, S.; Bollinger, J.-C.; Belkhir, L.; Tiri, A.; Bouzaza, A.; El Jery, A.; Assadi, A.; Amrane, A.; Mouni, L. Zeolite Waste Characterization and Use as Low-Cost, Ecofriendly, and Sustainable Material for Malachite Green and Methylene Blue Dyes Removal: Box–Behnken Design, Kinetics, and Thermodynamics. *Appl. Sci.* **2022**, *12*, 7587. [[CrossRef](#)]
53. Karoui, S.; Abou Saoud, W.; Ghorbal, A.; Fourcade, F.; Amrane, A.; Assadi, A.A. Intensification of non-thermal plasma for aqueous Ciprofloxacin degradation: Optimization study, mechanisms, and combined plasma with photocatalysis. *J. Water Process Eng.* **2022**, *50*, 103207. [[CrossRef](#)]
54. Abdellaoui, Y.; Abou Oualid, H.; Hsini, A.; El Ibrahim, B.; Laabd, M.; Ouardi, M.; Giacomani Vallejos, G.; Melo, P. Synthesis of Zirconium-Modified Merlinoite from Fly Ash for Enhanced Removal of Phosphate in Aqueous Medium: Experimental Studies Supported by Monte Carlo/SA Simulations. *Chem. Eng. J.* **2021**, *404*, 126600. [[CrossRef](#)]
55. Ouahiba, E.; Chabani, M.; Assadi, A.A.; Abdeltif, A.; Florence, F.; Souad, B. Mineralization and photodegradation of oxytetracycline by UV/H<sub>2</sub>O<sub>2</sub>/Fe<sup>2+</sup> and UV/PS/Fe<sup>2+</sup> process: Quantification of radicals. *Res. Chem. Intermed.* **2023**, *49*, 1–21. [[CrossRef](#)]
56. Ayoub, H.; Kassir, M.; Raad, M.; Bazzi, H.; Hijazi, A. Effect of Dye Structure on the Photodegradation Kinetic Using TiO<sub>2</sub> Nanoparticles. *J. Mater. Sci. Chem. Eng.* **2017**, *5*, 31–45. [[CrossRef](#)]
57. Gaya, U.; Abdullah, A. Heterogeneous Photocatalytic Degradation of Organic Contaminants Over Titanium Dioxide: A Review of Fundamentals, Progress and Problems. *J. Photochem. Photobiol. C Photochem. Rev.* **2008**, *9*, 1–12. [[CrossRef](#)]
58. Zeghioud, H.; Assadi, A.A.; Khellaf, N.; Djelal, H.; Amrane, A.; Rtimi, S. Reactive species monitoring and their contribution for removal of textile effluent with photocatalysis under UV and visible lights: Dynamics and mechanism. *J. Photochem. Photobiol. A Chem.* **2018**, *365*, 94–102. [[CrossRef](#)]
59. Katsumata, H.; Sakai, T.; Suzuki, T.; Knaeco, S. Highly Efficient Photocatalytic Activity of G-C<sub>3</sub>N<sub>4</sub>/Ag<sub>3</sub>PO<sub>4</sub> Hybrid Photocatalysts through Z-Scheme Photocatalytic Mechanism under Visible Light. *Ind. Eng. Chem. Res.* **2014**, *53*, 8018–8025. [[CrossRef](#)]
60. Li, H.; Zhang, D.; Han, X.; Xing, B. Adsorption of Antibiotic Ciprofloxacin on Carbon Nanotubes: PH Dependence and Thermodynamics. *Chemosphere* **2013**, *95*, 150–155. [[CrossRef](#)]
61. Kaouah, F.; Boumaza, S.; Berrama, T.; Trari, M.; Bendjama, Z. Preparation and Characterization of Activated Carbon from Wild Olive Cores (Oleaster) by H<sub>3</sub>PO<sub>4</sub> for the Removal of Basic Red 46. *J. Clean. Prod.* **2013**, *54*, 296–306. [[CrossRef](#)]
62. Baaloudj, O.; Nasrallah, N.; Kebir, M.; Khezami, L.; Amrane, A.; Assadi, A.A. A comparative study of ceramic nanoparticles synthesized for antibiotic removal: Catalysis characterization and photocatalytic performance modeling. *Environ. Sci. Pollut. Res.* **2021**, *28*, 13900–13912. [[CrossRef](#)] [[PubMed](#)]
63. Kenfoud, H.; Baaloudj, O.; Nasrallah, N.; Bagtache, R.; Assadi, A.A.; Trari, M. Structural and electrochemical characterizations of Bi<sub>12</sub>CoO<sub>20</sub> sillenite crystals: Degradation and reduction of organic and inorganic pollutants. *J. Mater. Sci. Mater. Electron.* **2021**, *32*, 16411–16420. [[CrossRef](#)]

**Disclaimer/Publisher’s Note:** The statements, opinions and data contained in all publications are solely those of the individual author(s) and contributor(s) and not of MDPI and/or the editor(s). MDPI and/or the editor(s) disclaim responsibility for any injury to people or property resulting from any ideas, methods, instructions or products referred to in the content.